12. D. N. Schmidt, H. R. Thierstein, J. Bollmann, in preparation.
13. G. Chapelle, L. S. Peck, *Nature* **399**, 114 (1999).
14. Materials and methods are available as supporting material on *Science* Online.
15. S. M. Stanley, *Evolution* **27**, 1 (1973).
16. S. J. Gould, *J. Paleontol.* **62**, 319 (1988).
17. R. Cifelli, *Syst. Zool.* **18**, 154 (1969).
18. R. D. Norris, *Paleobiology* **17**, 388 (1991).
19. H. P. Luterbacher, I. Premoli-Silva, *Rev. Ital. Paleontol. Stratigr.* **70**, 67 (1964).
20. A. D. Hecht, *J. Foram. Res.* **6**, 295 (1976).
21. S. Mulitza, A. Dürkoop, W. Hale, G. Wefer, H. S. Niebler, *Geology* **25**, 335 (1997).
22. G. Wefer, W. H. Berger, J. Bijma, G. Fischer, in *Use of*

Proxies in Paleoceanography, G. Fischer, G. Wefer, Eds. (Springer, Berlin, 1999), pp. 1–68.
23. J. C. Zachos, M. Pagani, L. Sloan, E. Thomas, K. Billups, *Science* **292**, 686 (2001).
24. J. H. Lipps, *Evolution* **24**, 1 (1970).
25. P. N. Pearson *et al.*, *Nature* **413**, 481 (2001).
26. E. Vincent, W. H. Berger, in *The Sea*, C. Emiliani, Ed. (Wiley, New York, 1981), vol. 7, pp. 1035–1119.
27. K.-Y. Wei, J. P. Kennett, *Paleoceanography* **1**, 67 (1986).
28. P. N. Pearson, M. R. Palmer, *Nature* **406**, 695 (2000).
29. K. G. MacLeod, B. T. Huber, T. Pletsch, U. Röhl, M. Kucera, *Paleoceanography* **16**, 133 (2001).
30. S. L. D'Hondt, M. A. Arthur, *Paleoceanography* **10**, 123 (1995).
31. M. Knappertsbusch, A. Mackensen, and R. Norris gener-

Widespread Intense Turbulent Mixing in the Southern Ocean

Alberto C. Naveira Garabato,[1]* Kurt L. Polzin,[2] Brian A. King,[3] Karen J. Heywood,[1] Martin Visbeck[4]

Observations of internal wave velocity fluctuations show that enhanced turbulent mixing over rough topography in the Southern Ocean is remarkably intense and widespread. Mixing rates exceeding background values by a factor of 10 to 1000 are common above complex bathymetry over a distance of 2000 to 3000 kilometers at depths greater than 500 to 1000 meters. This suggests that turbulent mixing in the Southern Ocean may contribute crucially to driving the upward transport of water closing the ocean's meridional overturning circulation, and thus needs to be represented in numerical simulations of the global ocean circulation and the spreading of biogeochemical tracers.

The meridional overturning circulation (MOC) results primarily from downwelling at a few selected regions in the North Atlantic and the Southern Ocean and from upwelling elsewhere in the ocean (*1*, *2*). Precisely where and at what rate this upwelling occurs, and what physical processes drive it, are poorly known variables that seriously limit the physical relevance of ocean circulation models under present and changed climate conditions (*2*). If the MOC is primarily closed by diapycnal turbulent mixing, an advective/diffusive model (*1*) implies a globally averaged diapycnal diffusivity K_ρ of 10^{-4} m^2 s^{-1} below ~1000 m. In contrast, observations of turbulence (*3*) and dye diffusion (*4*) in the open ocean pycnocline (above ~1000 m) have revealed background diffusivities that are an order of magnitude smaller. This motivated proposals that upwelling may be primarily effected by mesoscale eddies acting on the southward-shoaling isopycnals of the Southern Ocean (*5–7*). In recent years, however, large ($K_\rho \geq 10^{-4}$ m^2 s^{-1}) diapycnal diffusivities have been shown to occur over rough topography (*8*, *9*). But an assessment of whether topographi-

cally enhanced mixing can account for a globally averaged diffusivity of 10^{-4} m^2 s^{-1} at any depth is prevented by the difficulty of direct measurements of diapycnal mixing, with vast regions of the ocean (notably, the Southern Ocean) remaining essentially unsampled.

We used a novel technique (*10*) to begin filling the void of diapycnal mixing observa-

tions in the Southern Ocean. The technique enables us to estimate profiles of K_ρ from observed profiles of temperature, salinity, pressure, and current velocity (*11*). It relies on the premise that turbulent mixing at scales of a centimeter or less can be related to the more easily measured intensity of internal waves, whose nonlinear interaction initiates an energy cascade to smaller scales that results in turbulent mixing (*12*, *13*). Internal wave intensity is quantified in terms of vertical gradients of density and horizontal velocity on a scale of tens to hundreds of meters. Our study focuses on the southeast Pacific/southwest Atlantic sector of the Southern Ocean, where a total of 346 profiles of the required variables were obtained during five different cruises between 1993 and 1999 (colored diamonds in Fig. 1).

The study region hosts a wide range of bathymetric and oceanographic conditions. Bottom topography is characterized by a series of nearly featureless, well-sedimented abyssal plains in the southeast Pacific and is much more complex in the southwest Atlantic (Fig. 1). There, the geologically recent separation of the South American and Antarctic plates has given
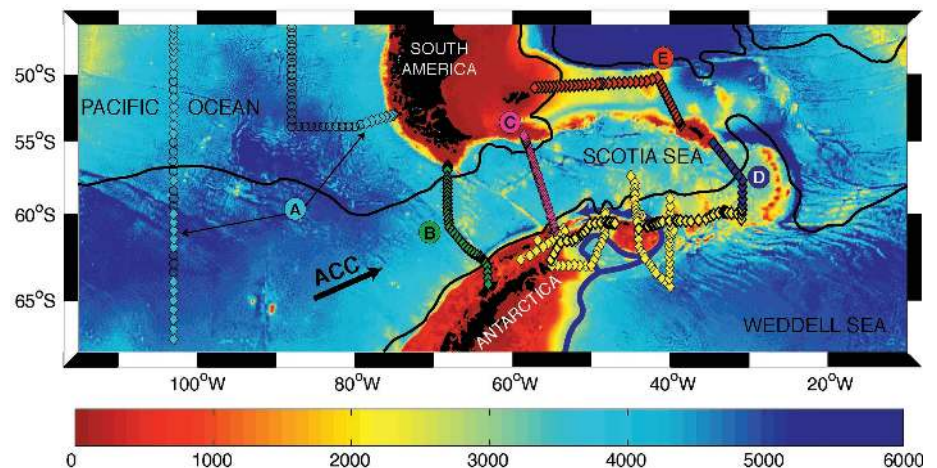
[1]School of Environmental Sciences, University of East Anglia, Norwich NR4 7TJ, UK. [2]Woods Hole Oceanographic Institution, Woods Hole, MA 02543, USA. [3]Southampton Oceanography Centre, Southampton SO14 3ZH, UK. [4]Lamont-Doherty Earth Observatory, Palisades, NY 10964–8000, USA.

*To whom correspondence should be addressed. E-mail: a.naveira-garabato@uea.ac.uk

Fig. 1. Bathymetry (*43*) of the study region. CTD/LADCP stations used in this study are shown by colored diamonds. Bold diamonds mark the section plotted in Fig. 2, with colors and circled letters denoting the stations used in constructing the panels in Fig. 3 (stations indicated by yellow diamonds were not used in Fig. 3). Open circles mark stations where only CTD data are available (these were used in strain calculations). The black lines indicate the northern and southern boundaries (*44*) of the ACC, whose direction of flow is indicated by the black arrow. The thick blue arrow marks the path of the deep boundary current transporting Antarctic Bottom Water from the Weddell Sea into the Scotia Sea (*25*).

rise to an area of rough sea floor, the Scotia Sea (*14*). This region is bounded to the west by Drake Passage and elsewhere by a system of ridges collectively referred to as the Scotia Ridge. The Scotia Sea is crisscrossed by a number of fracture zones and ridges that delimit small basins often textured with abyssal hills. Pronounced topographic features are present north of the Scotia Sea too, but the sea floor there is older and richer in sediment and consequently smoother. The study region is traversed by the eastward-flowing Antarctic Circumpolar Current (ACC) (Fig. 1), whose deep-reaching frontal jets experience strong wind forcing, interact with bottom topography, and generate substantial mesoscale eddy activity (*15*). Stratification weakens notably in crossing the ACC southward, with buoyancy frequency decreasing by about a factor of 2 at mid-depth, and is generally low by global standards except at the pycnocline near 200 m.

The spatial distribution of mixing in the Southern Ocean is exemplified by a section along the rim of the Scotia Sea (Fig. 2) (*16*). There is a striking relation between K_ρ and topographic roughness at length scales on the order of 10 km, reminiscent of microstructure observations at lower latitudes (*8*). Unlike in the latter, however, high values of around 10^{-4} m^2 s^{-1} or greater extend far from the topography and are surprisingly widespread below 500 to

1000 m over much of the section (*17*). The most intense mixing occurs over the rough sea floor of Drake Passage, the South Scotia Ridge, and the eastern Scotia Sea, where K_ρ increases from $\sim 10^{-4}$ m^2 s^{-1} at 500 m to 10^{-3} m^2 s^{-1} to 10^{-2} m^2 s^{-1} near the sea floor. Peak values of approximately 10^{-1} m^2 s^{-1} are observed at the bottom of Drake Passage and in a deep gap in the South Scotia Ridge. Comparatively low diffusivities of 4×10^{-5} m^2 s^{-1} to 4×10^{-4} m^2 s^{-1} occur over smoother bathymetry north of the Scotia Sea. In the uppermost 300 to 400 m throughout much of the section, there is a sharp reduction in K_ρ to values slightly above 10^{-5} m^2 s^{-1} that is related to the ubiquitous high stratification of the pycnocline. The influence of stratification is also apparent in a tendency of deep K_ρ contours to be aligned with isopycnals, a consequence of the southward decrease in buoyancy frequency across the ACC.

The dependence of the large-scale K_ρ distribution on stratification and topography is illustrated by Fig. 3. Over the abyssal plains of the southeast Pacific (Fig. 3A), low diffusivities of around 10^{-5} m^2 s^{-1} prevail throughout almost the entire water column, associated with low values of the turbulent kinetic energy dissipation rate ε (*13*) on the order of 10^{-10} W kg^{-1} that decrease with depth. These result in vertically integrated dissipation rates E (*18*) of 1×10^{-3} W m^{-2} to 2×10^{-3} W m^{-2}. As the ACC reaches

Drake Passage (Fig. 3B), stratification is essentially unchanged, but both ε and K_ρ increase by one to three orders of magnitude after the onset of rough topography. The depth trend of ε is reversed here and E is raised by an order of magnitude to 1×10^{-2} W m^{-2} to 3×10^{-2} W m^{-2}. A similar scenario is encountered in the central (Fig. 3C) and eastern (Fig. 3D) Scotia Sea, and it is only when the region of smoother topography north of the Scotia Sea is reached (Fig. 3E) that ε and K_ρ relax toward southeast Pacific values, with $E \sim 5 \times 10^{-3}$ W m^{-2}.

The uncertainty in K_ρ determined with the present method is estimated as a factor of 2 to 3 (*10*, *19*). Independent support for some features of the inferred distribution can be obtained from a number of sources. First, internal waves have a signature in stratification as well as in velocity shear. This signature can be quantified in terms of the measured variance of strain (*16*, *20*), the vertical gradient of isopycnal vertical displacement. The distribution of strain variance shows good qualitative agreement with that of K_ρ (*21*). Second, we obtained a second estimate of K_ρ using a technique (*22*) that relates mixing to the vertical structure of the turbulent overturns resulting from internal wave breaking. A scale analysis (*23*) predicts that these overturns should be detectable in density profiles if $K_\rho > 10^{-3}$ m^2 s^{-1}. Both K_ρ estimates agree to within the combined uncertainty of the two methods (a
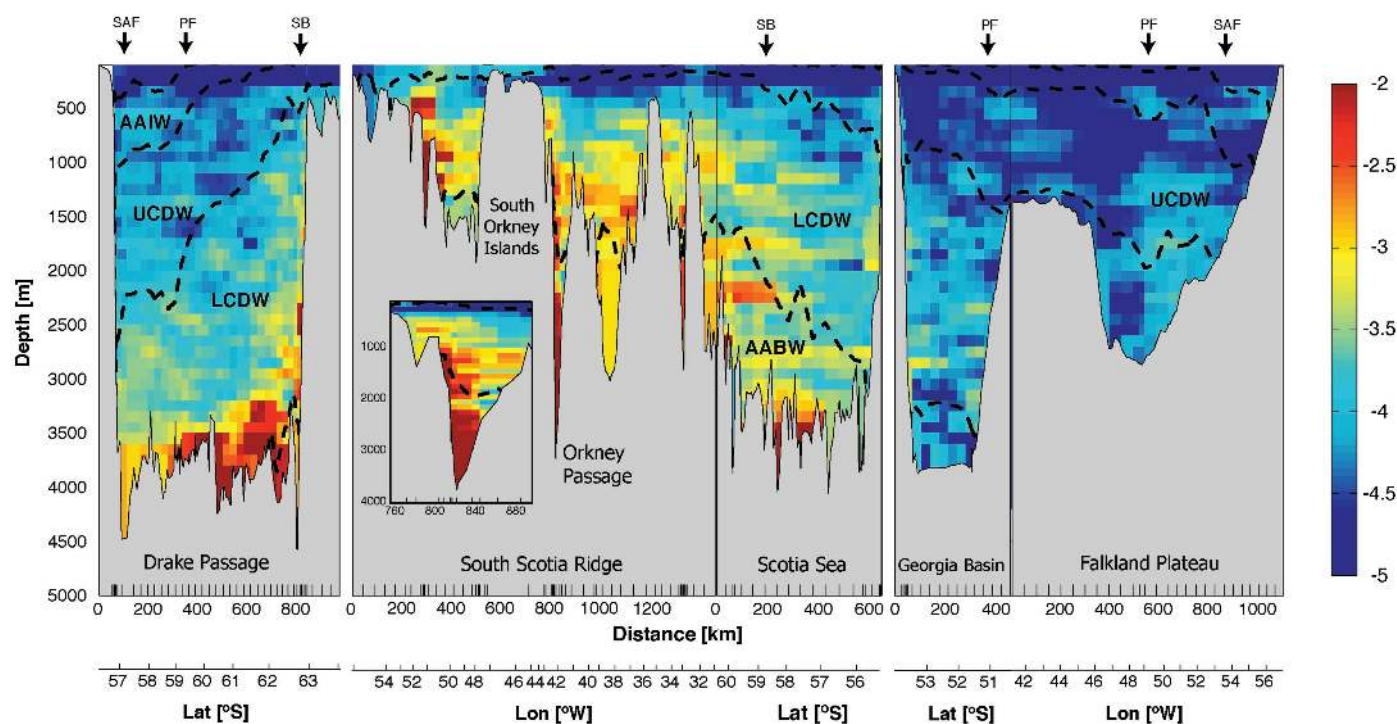

Fig. 2. Vertical distribution of $\log_{10}$ of K_ρ (in m^2 s^{-1}) following a section along the rim of the Scotia Sea (marked by bold diamonds in Fig. 1) anticlockwise. To improve the signal-to-noise ratio, K_ρ is calculated in 320-m bins by averaging data in groups of five adjacent stations. Density surfaces separating different water masses (AAIW, Antarctic Intermediate Water; UCDW and LCDW, Upper and Lower

Circumpolar Deep Water; AABW, Antarctic Bottom Water) are shown by the thick dashed lines. Crossings of the two main frontal jets of the ACC (SAF, Subantarctic Front, the ACC's northern boundary; PF, Polar Front) and its southern boundary (SB) are marked in the upper axis. Station positions are indicated by tick marks at the base of the topography. Lat, latitude; Lon, longitude.
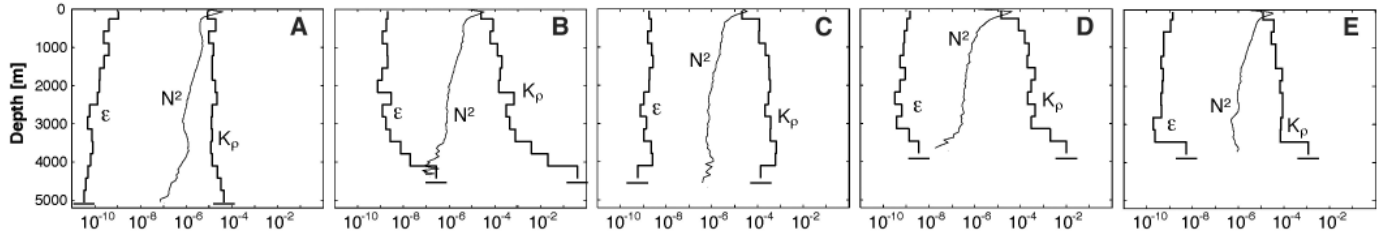
Fig. 3. Average profiles of N^2 (in s^{-2}), ε (in W kg^{-1}), and K_ρ (in m^2 s^{-1}) following the ACC through the study region (the stations used in constructing each of the panels are marked in Fig. 1). (**A**) Southeast Pacific, (**B**) western Drake Passage, (**C**) central Scotia Sea, (**D**) eastern Scotia Sea; (**E**) north of the Scotia Sea. Horizontal lines indicate the factor of 3 uncertainty in ε and K_ρ. The mean vertically integrated dissipation rate E in areas deeper than 2000 m within each of these regions is as follows: (A) 2×10^{-3} W m^{-2}, (B) 2.0×10^{-2} W m^{-2}, (C) 1.4×10^{-2} W m^{-2}, (D) 1.0×10^{-2} W m^{-2}, and (E) 5×10^{-3} W m^{-2}.

factor of 3 to 4) with no significant bias. Third, deep diffusivities in excess of 10^{-2} m^2 s^{-1} are common along the path of the boundary current conveying newly ventilated Antarctic Bottom Water from the Weddell Sea into the Scotia Sea (thick blue arrow in Fig. 1). A scaling argument (*24*) suggests that they are of the right order of magnitude to close the abyssal heat budget of the Scotia Sea, which requires a basin-average abyssal K_ρ of $3.9 \pm 1 \times 10^{-3}$ m^2 s^{-1} (*25*). Finally, the only dedicated in situ measurement of mixing in the Southern Ocean to date (*26*) (an upper ocean tracer release experiment in the ACC south of New Zealand) yielded low K_ρ values in the range 1×10^{-5} m^2 s^{-1} to 3×10^{-5} m^2 s^{-1} near the base of the upper ocean mixed layer. This result concurs with the diffusivities determined in our study for the uppermost 300 m of the ACC region.

In order for the observed widespread high ε levels to be maintained, energy must be continuously supplied to the internal wave field. The visual link with bathymetric roughness in Figs. 2 and 3 suggests internal wave generation as flows impinge on rough topography as the primary energy source of the enhanced mixing. Whether those flows are of tidal or geostrophic origin cannot be ascertained here, but larger mean and eddy flows and farther penetration of high dissipations into the water column [relative to the Brazil Basin (*8, 27*)] hint (*28*) at a greater importance of geostrophic sources than at lower latitudes. This suggestion is reinforced by vertically integrated dissipation rates in the Scotia Sea ($E \sim 1 \times 10^{-2}$ W m^{-2} to 3×10^{-2} W m^{-2}), comparing well with the rate of working by the wind on the ACC [$\sim10^{-2}$ W m^{-2} (*29*)] and exceeding tidally driven values in the Brazil Basin by nearly an order of magnitude (*27*) despite the Scotia Sea hosting smaller tidal velocities. Bottom internal wave generation in regions of high mixing is supported by rotary spectra of vertical shear (*21*). These display a dominance of clockwise over counterclockwise shear variance below 500 to 1000 m, which in the Southern Hemisphere denotes upward propagation of internal wave energy (*30*). In the upper ocean, however, and in areas of low and moderate mixing over benign topography, counterclockwise exceeds clockwise shear variance and suggests a dominance of wind-induced near-inertial waves. Vertically integrated dissipation rates in these areas (1×10^{-3} W m^{-2} to 3×10^{-3} W m^{-2}) are indeed comparable in magnitude to regional estimates of the energy flux from the wind to near-inertial motions in the upper ocean mixed layer (*31*).

The wide range of bathymetric and oceanographic environments in our study region arguably make it a microcosm of mixing conditions in much of the deep Southern Ocean. We anticipate that other ACC regions of young, rough sea floor will host mixing levels close to those observed in the Scotia Sea. Candidates include the environs of the Mid-Atlantic and Southwest Indian Ridges, the Kerguelen Plateau (*32*), the Southeast Indian Ridge, and the Pacific Antarctic Ridge. If much of the path of the ACC is seeded with hot spots of diapycnal mixing, our view of the MOC closure in the Southern Ocean and its energetics will change considerably. For example, larger exchanges of water between the shallow and deep cells of the MOC will be implied than previously thought possible (*33*), and much of the bottom water upwelling needed to close the deep cell of the MOC will occur within the Southern Ocean at the expense of the ocean basins to the north. Additionally, the strong spatial inhomogeneity of mixing could drive significant residual circulations (*2*) across the ACC that may relax the requirement for mesoscale eddy-driven transports to support the southward-flowing limb of the MOC (*34*). If the enhanced dissipation rates are maintained by geostrophic sources, as suggested here, the interaction of the ACC with bottom topography may prove to be an important sink of energy input by the wind into the oceanic general circulation, consistent with $\sim80\%$ of the global input occurring in the Southern Ocean (*29, 35*). Our observations highlight the potentially key contribution of turbulent mixing in the Southern Ocean to closing the MOC, and raise a number of questions on energy sources and coupling to mean and eddy flows that only a large dedicated observational and modeling effort will be able to answer.

References and Notes
1. W. Munk, C. Wunsch, *Deep-Sea Res. I* **45**, 1977 (1998).
2. C. Wunsch, R. Ferrari, *Annu. Rev. Fluid Mech.*, in press.
3. M. C. Gregg, *J. Geophys. Res.* **92**, 5249 (1987).
4. J. R. Ledwell, A. J. Watson, C. S. Law, *J. Geophys. Res.* **103**, 21499 (1998).
5. J. R. Toggweiler, B. Samuels, *J. Phys. Oceanogr.* **28**, 1832 (1998).
6. D. J. Webb, N. Suginohara, *Nature* **409**, 37 (2001).
7. C. W. Hughes, *Nature* **416**, 136 (2002).
8. K. L. Polzin, J. M. Toole, J. R. Ledwell, R. W. Schmitt, *Science* **276**, 93 (1997).
9. J. R. Ledwell *et al.*, *Nature* **403**, 179 (2000).
10. K. Polzin, E. Kunze, J. Hummon, E. Firing, *J. Atmos. Oceanic Technol.* **19**, 205 (2002).
11. Profiles of temperature, salinity, and pressure were obtained with a CTD (conductivity-temperature-depth) instrument. Current velocity was measured with a lowered acoustic Doppler current profiler (LADCP) mounted on the CTD package.
12. C. Garrett, *Nature* **422**, 477 (2003).
13. In a statistically stationary internal wave field, the rates at which internal wave breaking dissipates kinetic energy and induces diapycnal mixing (expressed as a turbulent dissipation ε and a diapycnal diffusivity K_ρ, respectively) are related by a turbulent production/dissipation balance of the form $P = \varepsilon + K_\rho N^2$, where P is turbulent production and N is the buoyancy frequency. The term $K_\rho N^2$ represents the diapycnal buoyancy flux associated with mixing and is assumed to be a constant fraction ($R_f = 0.15$) of P, so that $K_\rho = R_f/(1 - R_f) \times (\varepsilon/N^2)$ (*36*). Our calculation of ε equates P to the downscale energy transport arising from internal wave-wave interactions, resulting in the expression $\varepsilon = \varepsilon_0 \times (f/f_0) \times [\cosh^{-1}(N/f)/\cosh^{-1}(N_0/f_0)] \times (N^2/N_0^2) \times (\langle V_z^2 \rangle/\langle V_{z-GM}^2 \rangle) \times F(R_\omega)$ (*37*). Here, $\varepsilon_0 = 7.8 \times 10^{-10}$ W kg^{-1} is the turbulent dissipation predicted for the Garrett and Munk (GM) model of the background internal wave field in stratification defined by a buoyancy frequency $N_0 = 5.24 \times 10^{-3}$ rad s^{-1} at 30° latitude (*38*). f_0 and f are the inertial frequencies at 30° and the latitude of observation, respectively. N denotes the buoyancy frequency calculated from CTD observations. $\langle V_z^2 \rangle$ is the variance of the N-normalized LADCP vertical shear, and $\langle V_{z-GM}^2 \rangle$ is the corresponding variable predicted by the GM model. $F(R_\omega)$ is a known function of the frequency content of the internal wave field (*37, 39*) and is estimated from the shear-to-strain ratio R_ω [defined in (*16*)].
14. R. A. Livermore, R. W. Woollett, *Earth Planet. Sci. Lett.* **117**, 475 (1993).
15. S. R. Rintoul, C. W. Hughes, D. J. Olbers, in *Ocean Circulation and Climate: Observing and Modelling the Global Ocean*, G. Siedler, J. Church, J. Gould, Eds. (Academic Press, London, 2001), pp. 271–302.
16. To construct Figs. 2 and 3, each LADCP velocity shear profile was divided into overlapping 320-m segments centered at equally spaced depths and normalized by the segment-averaged N. The normalized shear in each segment was Fourier-transformed (64 points) and its vertical wavenumber power spectral density was computed. This spectrum was then corrected (*10*) to account for attenuation resulting from the spatial averaging inherent in LADCP measurement and data processing. $\langle V_z^2 \rangle$ was calculated as the corrected power spectral density integrated between a maximum vertical wavelength of 320 m and a variable minimum vertical wavelength that ranged from 50 to 90 m. This minimum value was determined for each individual segment as the wavelength at which the ratio of the instrumental shear noise spectrum (modeled as a blue spectrum proportional to the squared vertical wavenum-

ber) to the measured shear spectrum equaled 1/3. This threshold was selected heuristically, and the resulting ε and K_ρ are insensitive to the exact choice of value. $\langle V_{z\text{-GM}}{}^2 \rangle$ was computed by integrating the GM N-normalized shear spectrum within the same wavelengths as for $\langle V_z{}^2 \rangle$. To estimate F (R_ω), a bulk shear-to-strain ratio (37) was diagnosed as $R_\omega = \langle V_z{}^2 \rangle / (N^2 \langle \xi_z{}^2 \rangle)$. Here, $\langle \xi_z{}^2 \rangle$ is the variance of strain, the vertical gradient in the vertical displacement of isopycnals induced by internal waves. We estimated strain from CTD density profiles using a scale separation assumption (20) and calculated $\langle \xi_z{}^2 \rangle$ (and R_ω) in 320-m segments identical to $\langle V_z{}^2 \rangle$ bins. Despite being somewhat noisy, the resulting R_ω distribution shows a consistent mean value of 8 to 12 between different regions and cruises. We thus used a constant F (R_ω) of 1/3 throughout the analysis. That value is a conservative choice based on an internal wave dynamical model (39) validated with microstructure observations (37).

17. Our in situ estimates of widespread large K_ρ values show some resemblance to diapycnal diffusivities diagnosed by an inverse calculation using ACC hydrographic observations (40).

18. The vertically integrated dissipation rate E is calculated as $\int \rho \varepsilon dz$, where ρ is the in situ density, and the integral spans the entire water column.

19. This factor is assumed to include temporal variability, as suggested by the analysis of three repeats of the eastern Drake Passage transect (Fig. 1, station C) yielding very similar diffusivities.

20. C. Mauritzen, K. L. Polzin, M. S. McCartney, R. C. Millard, D. E. West-Mack, *J. Geophys. Res.* **107**, 3147 (2002).

21. A. C. Naveira Garabato, K. L. Polzin, B. A. King, K. J. Heywood, M. Visbeck, data not shown.

22. T. D. Finnigan, D. S. Luther, R. Lukas, *J. Phys. Oceanogr.* **32**, 2988 (2002).

23. Our ability to detect turbulent overturns in density profiles is limited by the vertical and density resolutions of the CTD system. A spectral analysis of the vertical variability of N^2 reveals that the vertical resolution is ~15 m, a consequence of the heaving of the package in the large Southern Ocean swell. The density resolution was determined as 10^{-3} kg m^{-3} from inspection of low-N data segments. Given that the vertical resolution is often the limiting factor in our data set, an estimate of how energetic the turbulence needs to be for turbulent overturns to be resolved can be made. Using a scaling argument (22), the root mean square overturn scale (the Thorpe scale, L_T) can be related to a dissipation scale [the Ozmidov scale, $L_O = (\varepsilon/N^3)^{1/2}$] by a constant of proportionality close to unity; that is, $L_T \sim L_O$. Empirically, L_T has been shown to be a factor of $\pi - 2\pi$ smaller than the vertical scales of overturns, so we expect to resolve L_T values of ~5 m. Thus, from (13) and the expression for L_O, the minimum diapycnal diffusivity resolved by an overturn analysis will be $K_\rho = R_f/(1 - R_f) \times (\varepsilon/N^2) \sim R_f/(1 - R_f) \times (L_T{}^2 N) \sim 10^{-3}$ m^2 s^{-1}, where a value of $N \sim 7 \times 10^{-4}$ s^{-1} typical of the deep Southern Ocean has been used.

24. Our results suggest that the diapycnal mixing required to close the abyssal heat budget of the Scotia Sea (25) occurs in two distinct regimes. In the interior of the basin, K_ρ at the neutral density surface (28.31 kg m^{-3}) used in the abyssal heat budget is in the range $K_\rho{}^{int} \approx 2 \times 10^{-4}$ m^2 s^{-1} to 2×10^{-3} m^2 s^{-1}, whereas it is one to two orders of magnitude larger ($K_\rho{}^{dbc} \approx 5 \times 10^{-3}$ m^2 s^{-1} to 5×10^{-1} m^2 s^{-1}) in the deep boundary current conveying Antarctic Bottom Water into the basin and along its southern boundary (Fig. 1). Taking intermediate values of $K_\rho{}^{int}$ and $K_\rho{}^{dbc}$ and assuming that our sampling locations are representative, $K_\rho{}^{dbc}$ should apply over around one-tenth of the control area to produce a basin-average $K_\rho{}^{av}$ of $3.9 \pm 1 \times 10^{-3}$ m^2 s^{-1}. The resulting area (~7×10^4 km^2) broadly corresponds with that of the deep boundary current in our hydrographic observations north of the South Scotia Ridge (Fig. 1), although the uncertainty in this scaling argument is large (greater than a factor of 3).

25. K. J. Heywood, A. C. Naveira Garabato, D. P. Stevens, *Nature* **415**, 1011 (2002).

26. C. S. Law, E. R. Abraham, A. J. Watson, M. I. Liddicoat, *J. Geophys. Res.* **108**, 3272 (2003).

27. K. L. Polzin, *J. Phys. Oceanogr.*, in press.

28. K. L. Polzin, in *Internal Wave Modelling: Proceedings, 'Aha Huliko'a Hawaiian Winter Workshop*, P. Müller, D. Henderson, Eds. (special publication of the School of Ocean and Earth Science and Technology, Univ. of Hawaii, Honolulu, HI, 1999), pp. 117–128.

29. C. Wunsch, *J. Phys. Oceanogr.* **28**, 2332 (1998).

30. K. D. Leaman, T. B. Sanford, *J. Geophys. Res.* **15**, 1975 (1975).

31. M. H. Alford, *Geophys. Res. Lett.* **30**, 1424 (2003).

32. An application of an earlier version of our technique to 12 LADCP velocity profiles downstream of the Kerguelen Plateau (41) indeed revealed enhanced ($K_\rho \geq 10^{-4}$ m^2 s^{-1}) diapycnal mixing in the region below a depth of 500 to 1000 m.

33. K. Speer, S. R. Rintoul, B. M. Sloyan, *J. Phys. Oceanogr.* **30**, 3212 (2000).

34. This is exemplified by the high sensitivity of the Southern Ocean MOC in a zonal channel model to the prescribed diapycnal buoyancy flux divergence (42).

35. Near-local dissipation of the ~8×10^{11} W input by the wind into the Southern Ocean general circulation would imply an ACC-mean vertically integrated dissipation rate $E \sim 10^{-2}$ W m^{-2} (29). If representative of other regions, our inference of $E \sim 1 \times 10^{-2}$ W m^{-2} to 3×10^{-2} W m^{-2} in the Scotia Sea and near the Kerguelen Plateau (28), combined with background values an order of magnitude smaller, indicates that diapycnal mixing hot spots would need to occupy a substantial fraction (roughly one-third) of the ACC region to dissipate the bulk of the wind work. The abundance of complex topography along the current's path suggests that an energy budget closure of this type may apply.

36. T. R. Osborn, *J. Phys. Oceanogr.* **20**, 83 (1980).

37. K. L. Polzin, J. M. Toole, R. W. Schmitt, *J. Phys. Oceanogr.* **25**, 306 (1995).

38. C. J. R. Garrett, W. H. Munk, *J. Geophys. Res.* **80**, 291 (1975).

39. E. S. Henyey, J. Wright, S. M. Flatté, *J. Geophys. Res.* **91**, 8487 (1986).

40. D. Olbers, M. Wenzel, in *Oceanic Circulation Models: Combining Data and Dynamics*, D. L. T. Anderson, J. Willebrand, Eds. (Kluwer Academic, Dordrecht, Netherlands, 1989), pp. 95–139.

41. K. L. Polzin, E. Firing, *Int. WOCE Newsl.* **29**, 39 (1997).

42. R. H. Karsten, H. Jones, J. Marshall, *J. Phys. Oceanogr.* **32**, 39 (2003).

43. W. H. F. Smith, D. T. Sandwell, *Science*, **277**, 1956 (1997).

44. A. H. Orsi, T. Whitworth, W. D. Nowlin, *Deep-Sea Res. I* **42**, 641 (1995).

45. A Natural Environment Research Council postdoctoral research fellowship supported A.C.N.G. during the analysis and writing of this report. Feedback from L. Goldson, E. Kunze, R. Muench, K. Oliver, B. Sloyan, K. Speer, K. Stansfield, A. Watson, and two anonymous reviewers is gratefully acknowledged.

Virus-Based Toolkit for the Directed Synthesis of Magnetic and Semiconducting Nanowires

Chuanbin Mao,[1]* Daniel J. Solis,[4]* Brian D. Reiss,[5]
Stephen T. Kottmann,[4] Rozamond Y. Sweeney,[2] Andrew Hayhurst,[2]
George Georgiou,[2,3] Brent Iverson,[1,2] Angela M. Belcher[5]†

We report a virus-based scaffold for the synthesis of single-crystal ZnS, CdS, and freestanding chemically ordered CoPt and FePt nanowires, with the means of modifying substrate specificity through standard biological methods. Peptides (selected through an evolutionary screening process) that exhibit control of composition, size, and phase during nanoparticle nucleation have been expressed on the highly ordered filamentous capsid of the M13 bacteriophage. The incorporation of specific, nucleating peptides into the generic scaffold of the M13 coat structure provides a viable template for the directed synthesis of semiconducting and magnetic materials. Removal of the viral template by means of annealing promoted oriented aggregation-based crystal growth, forming individual crystalline nanowires. The unique ability to interchange substrate-specific peptides into the linear self-assembled filamentous construct of the M13 virus introduces a material tunability that has not been seen in previous synthetic routes. Therefore, this system provides a genetic toolkit for growing and organizing nanowires from semiconducting and magnetic materials.

The reliance of future technologies on developing scalable and economic methods for the fabrication of one-dimensional (1D) systems has spurred intense and rapid progress in the area of materials synthesis. In particular, 1D materials have been enthusiastically pursued for their applications in the study of electrical transport (1), optical phenomena (2), and as functional units in nanocircuitry (3). Pursuit of "bottom-up" methods for the synthesis of semiconducting, metallic, and magnetic nanowires has yielded strategies including, but not limited to, vapor liquid solid (VLS) (4), chemical (5), solvothermal, vapor phase, and template-directed fabrication (6). Although each method developed for the production of nanowires has had success in achieving high-quality materials, no distinct strategy to date has yielded monodisperse, crystalline nanowires of radically different compositions. The realization of such a system

[1]Departments of Chemistry and Biochemistry, [2]Institute for Cellular and Molecular Biology, [3]Department of Chemical Engineering, University of Texas (UT) at Austin, Austin, TX 78712, USA. [4]Department of Chemistry, [5]Department of Materials Science and Engineering and Biological Engineering Division, Massachusetts Institute of Technology (MIT), Cambridge, MA 02139–4307, USA.

*These authors contributed equally to this work.
†To whom correspondence should be addressed. E-mail: belcher@mit.edu